

Investigating magma ocean solidification on Earth through laser-heated diamond anvil cell experiments

**Farhang Nabiei^{1, 2}, James Badro^{3, 1}, Charles-Édouard Boukaré^{1, 3}, Cécile Hébert², Marco
Cantoni⁴, Stephan Borensztajn³, Nicolas Wehr³, Philippe Gillet¹**

¹Earth and planetary science laboratory, EPFL, Lausanne, Switzerland

²Electron spectrometry and microscopy laboratory, EPFL, Lausanne, Switzerland

³Université de Paris, Institut de physique du globe de Paris, CNRS, Paris, France

⁴Interdisciplinary Centre for Electron Microscopy, EPFL, Lausanne, Switzerland

Contents of this file

Text S1 to S7

Figures S1 to S10

Tables S1 to S3

1. Methods

a. LHDAC experiments

A total of five experiments were performed using the laser-heated diamond anvil cell. Re gaskets were indented at 20 GPa to a thickness of $\sim 40 \mu\text{m}$ using $300 \mu\text{m}$ diamond culets, and then drilled using a picosecond laser machining instrument (IPGP) to a diameter of $120 \mu\text{m}$. Three experiments were performed with natural coarse-grained San Carlos olivine. Two experiments were performed with a synthetic glass having a simplified pyrolitic composition (Table S1) produced in a gas-mixing ($\text{Ar-CO}_2\text{-H}_2$) aerodynamic levitation laser furnace (IPGP), operating at 2050°C and an oxygen fugacity of $\text{IW}+1.3$. This provides a final Fe^{3+} content in pyrolite comprised between 2.7% and 3.5%, consistent with upper mantle ferric iron concentration [Sossi *et al.* 2020] in peridotites.

Pressure in the diamond cell was measured by tracking the 1st order Raman peak of diamond [Akahama and Kawamura, 2010] in the center of the culet, in the same position where we the sample was laser heated.

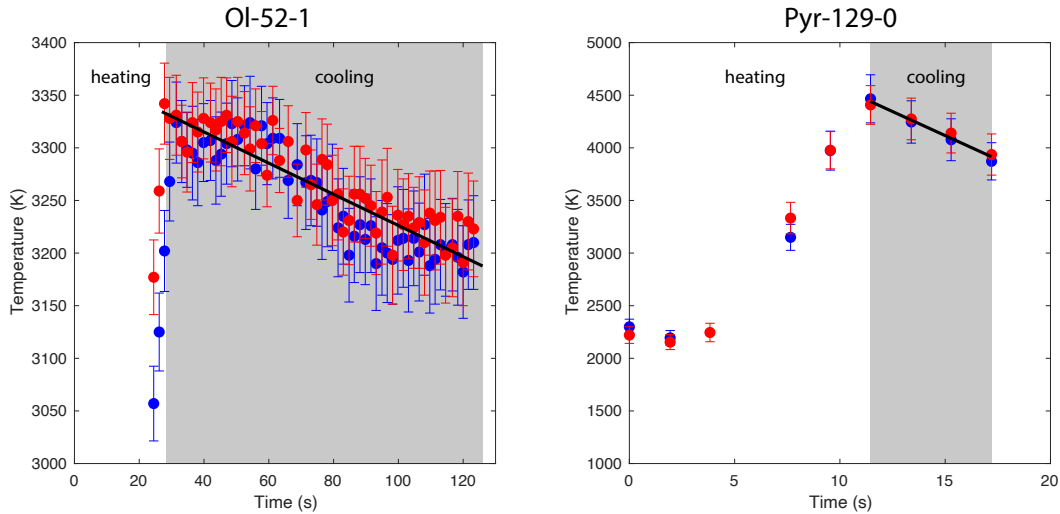


Figure S1: Two typical temperature vs. time (*i.e.* thermal histories) of samples produced in this work. The blue and red dots correspond to T measurements from either side. The white background corresponds to the heating phase above the solidus, and the grey background to the subsequent controlled cooling phase. OI-52-1 on the left was molten at 52 GPa and $3350 \pm 50 \text{ K}$ and cooled slowly to $3200 \pm 50 \text{ K}$ over the course of 1.5 minutes at a cooling rate of 1.6 K/s, while Pyr-129-0 on the right was molten at 129 GPa and $4500 \pm 250 \text{ K}$ and rapidly cooled to $3900 \pm 200 \text{ K}$ over the course of 6 seconds at a cooling rate of 90 K/s.

The samples were heated using a double-sided laser heating instrument (IPGP). The two laser branches are linearly polarised, and each beam goes through a half-wave plate (that allows to rotate the polarisation) and a polariser. This allows to gradually modify the laser power delivered on each side by rotating its polarisation, independently. Before melting

the sample, we adjusted laser power on both sides to have identical temperatures, then power was ramped up uniformly from both sides until target T was reached above the solidus (Fig. S1). Then, we used different strategies to cool the samples down, depending on the cooling rate used (this ranges from 1.5 K/s to 90 K/s). For the faster cooling rates (Pyr-52-0, Pyr-85-0, Pyr-129-0), we dropped laser power by rotating the polarisation of the laser (from both sides simultaneously and uniformly). For the slower cooling rates (Pyr-52-1, Ol-52-1, Ol-52-3, Ol-52-6), we let laser power seep, and adjusted its uniformity by decreasing (if T dropped too slowly) or increasing (if T dropped too rapidly) laser power on the sample.

The samples were cooled over the course of 30 to 360 seconds (Fig. S1 and Table S1). Then temperature was quenched in a few tens of microseconds by shutting off the laser, and pressure was slowly released to recover the gasket and the sample for subsequent analysis.

Table S1: Pressure and temperature conditions of the experimental runs.

Sample no.	P (before heating) GPa	P (after heating) GPa	T (melting) K	T (final) K
Ol-52-1	44 \pm 2	52 \pm 4	3350 \pm 50	3200 \pm 50
Ol-52-3	44 \pm 2	52 \pm 4	3300 \pm 50	3090 \pm 50
Ol-52-6	44 \pm 2	52 \pm 4	3330 \pm 50	3030 \pm 50
Pyr-52-0	44 \pm 2	52 \pm 4	3430 \pm 50	3230 \pm 50
Pyr-52-1	44 \pm 2	52 \pm 4	3400 \pm 50	3200 \pm 50
Pyr-85-0	76 \pm 3	85 \pm 6	4100 \pm 200	3600 \pm 200
Pyr-129-0	119 \pm 5	129 \pm 8	4500 \pm 250	3900 \pm 200

Temperature was measured by spectroradiometry radiation on a central 10 microns area. This sampling corresponds to the size of the central residual melt for large melt fractions (Fig. S5), but is larger than that when melt fraction drops, so that we are averaging temperatures of the crystallised part as well. This is one of the limitations of our temperature measurements, and while the relative temperature changes that we record are trustworthy, the absolute temperature may be lower than the true temperature in the center of the sample. Also, the uncertainty of the absolute temperature in the DAC (Benedetti and Loubeyre, 2001) is in the 200–300K range between 3000 and 4000 K. Note that the precisions is much better than that, as seen from temperature monitoring of the samples (i.e. temperature vs. time plots, Fig. S1), and so are the statistical uncertainties of our measurements (error bars in Fig. S1).

We fit both the Planck and Wien functions and these are always within 5 % from each other. The wavelength range was between 500 and 750 nm, and temperature is constantly monitored from both sides simultaneously (Fig. S1).

b. 3D EDS acquisition and analysis

A Zeiss NVision 40 (Ol-52-3 and Ol-52-6) or Zeiss X540 (Ol-52-1, Pyr-52-0, Pyr-52-1, Pyr-85-0, Pyr-129-0) dual beam SEM-FIB instruments (EPFL) were used in this study. Both instruments are equipped with Oxford Instruments EDS detector. The sample was brought up to beam coincidence and tilted to be perpendicular to the ion beam. The interested area of the sample was initially coated with Pt. After milling the correction lines, the Pt coating was covered with a carbon layer. This gives a clear reference mark on the coating that is used for drift correction after the whole set of measurements. The front edge of the zone of interest was milled away until the molten part was reached. The materials next to the coated area toward the EDS detector was also removed to avoid any blocking and shadowing effect. 3D tomography and x-ray acquisition was started after having cleaned the surface. For each slice a secondary electron image and an EDS map was recorded by INCA (Ol samples) or Aztec (Pyr samples) software from Oxford Instruments and then one slice with the thickness between 50-150 nm (depending on the sample) was removed. The electron beam high voltage was set between 4 and 12 kV. This high-tension range is enough to record O L line at 0.54 keV, Si K line at 1.8 keV, Mg K line at 1.3 keV and Fe L line at 0.7 keV. About half of the heated area was used for slicing to produce 3D chemical model of the volume and the phases.

MultiStackReg and Template Matching plugins in ImageJ (Fiji) were used on the secondary electron image stacks to correct the drift based on the marker lines in the platinum deposition as a reference. Then, a transformation matrix or a small ImageJ macro was used to impose the same alignment for elemental maps. The intensity maps are combined in 2D as RGB images with red, green, and blue channels being Fe, Si, and Mg maps (Fig. 1, Fig. S9). Then, all the acquired maps were quantified with INCA or AZtec software. AutoIt script was written to facilitate the quantification for all the slices on INCA software and to save quantified elemental maps with atomic percentage for Mg, Si, and Fe. The quantified elemental maps were loaded to Mathematica for further image analysis and phase identifications. Segmentation was done by separating the image pixels based on the expected phase composition to make 3D representation for each phase. At the end, Avizo software from Thermo Fisher Scientific was used to visualize the 3D maps.

c. TEM preparation

The other half of the samples (except Ol-52-3) were used to make thin sections for transmission electron microscopy with the FIB lift-out technique. The front of the sample was empty after the 3D acquisition. The bulk of material behind the thin section, intended to be lifted-out, was milled away and the thin sections were transferred and glued to a copper probe with ion beam induced carbon deposition. The samples were then thinned with a 30 kV ion beam with currents ranging from 700 pA down to 80 pA. The final polishing was done with 5 kV and 30 pA ion beam to obtain thicknesses of around 100 nm. The TEM samples were about 20 μm in length and width, which is substantially larger than the usual sizes and that makes them difficult to thin evenly. Moreover, the residual strain in the sample caused them to start bending as soon as they get thin enough. We have employed windowed thinning, and fine localized thinning at low current and low voltage to overcome this problem and obtain wide electron-transparent areas to study. However, this resulted in uneven thickness in the thin sections.

d. STEM EDS

A Tecnai Osiris scanning transmission electron microscope (STEM) from Thermo Fisher Scientific equipped with four windowless Super-X SDD EDS detectors from Bruker was used for chemical analysis of the samples. The microscope was operated at 200 kV high tension in STEM mode to obtain bright field (BF) and high-angle annular dark field (HAADF) images. The EDS maps were acquired with 50-100 μ s dwell time for 400-1000 seconds to have a sufficient amount of counts. Quantification was done using the K lines of elements with the Cliff-Lorimer method, except for the concentration of oxygen which follows the stoichiometric ratios of the phases. This was done by built-in algorithm and parameters (k-factors, detector efficiency, etc.) of the Bruker Esprit 1.9 used for EDS analysis. There are two general types of error in this method of quantification. The first one comes from fitting Gaussians to the x-ray peaks to extract their intensities. This error is dominant when there is a low signal-to-noise ratio. The large areas of the detectors used in our experiments ensure a high count rate, thus, improving the signal-to-noise ratio. In addition, we have selected rectangular regions on the EDS maps to extract the sum spectrum for quantification. Care was taken to select these rectangles where a large portion of the target phase is available to increase the total number of counts in the rectangle. Therefore, the statistical error is always negligible and below 1%. The second type of error comes from the contribution of absorption and fluorescence which are neglected in the assumptions of the Cliff-Lorimer method. Generally speaking, this is a reasonable assumption for TEM EDS, as the thickness of the sample and the interaction volume are low. However, uneven thickness in our samples can be a source of error, and while it is not straightforward to directly calculate this, we estimated this error by using several maps and taking spectrums from different locations of the map, and used the average values as the composition of the target phase and the standard deviations as an indication of their uncertainty. This yields an uncertainty of 1–2% for high concentration elements (Mg and Si), and 8–10% for low-concentration elements (Fe, Al, Ca).

2. Analysis

a. Closed System

The sub-solidus region extends outwards in the temperature gradient with grain size continually getting smaller until it morphs into the untransformed starting material (Fig. S2). The composition of the sub-solidus region is identical to that of the untransformed starting material as can be seen from chemical analyses reported in Table S3. This indicates that the spherical melt pocket (which is the object of our study) has not leaked or exchanged any elements, and is chemically isolated from the outer parts of the sample. Thus, it can be treated as a chemically closed system.

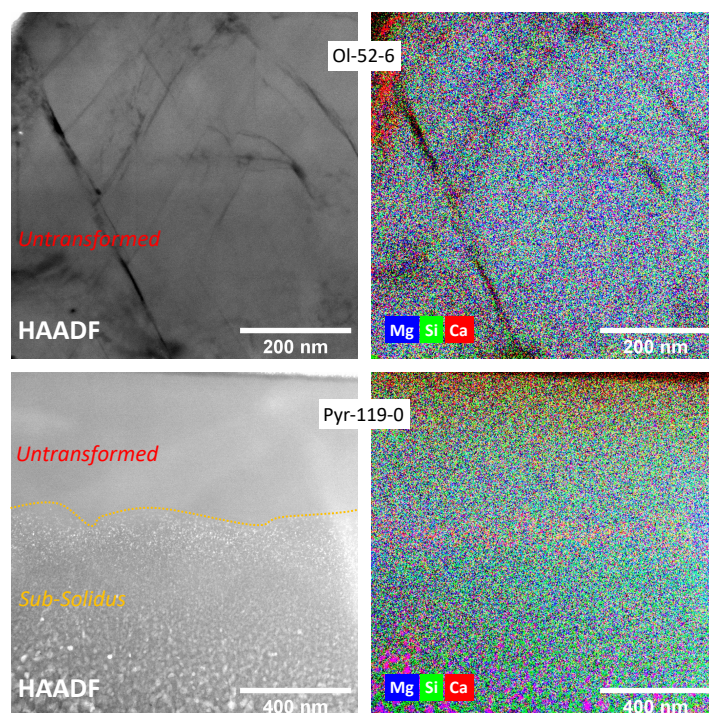


Figure S2: TEM images (left) and chemical analyses (right) of untransformed and subsolidus phase assemblage in two samples, OI-52-6 on top and Pyr-119-0 on the bottom. Such areas are all around the melt pocket, and can be chemically analysed and averaged to give the compositions reported in Table S2.

Table S2: Chemical composition of the untransformed and subsolidus phase assemblages for an olivine sample at 52 GPa, and two pyrolite samples (52 GPa and 129 GPa), determined by TEM EDS analyses. This shows that composition of the untransformed (*i.e.* starting) material is indistinguishable from that of the subsolidus phase.

Bulk composition		Composition (mol%)									
		MgO	σ	FeO	σ	SiO ₂	σ	Al ₂ O ₃	σ	CaO	σ
Olivine 52 GPa	<i>Untransformed</i>	58.65	0.57	7.20	0.72	34.15	0.36				
	<i>Subsolidus</i>	58.80	0.57	7.90	0.79	33.30	0.36				
Pyrolite 52 GPa	<i>Untransformed</i>	46.02	0.98	6.90	0.64	42.42	0.80	2.35	0.20	2.31	0.23
	<i>Subsolidus</i>	44.16	0.94	7.21	0.67	44.05	0.84	2.28	0.19	2.28	0.23
Pyrolite 129 GPa	<i>Untransformed</i>	45.70	0.80	6.66	0.32	43.13	0.44	2.38	0.02	2.14	0.04
	<i>Subsolidus</i>	46.62	0.25	6.36	0.34	42.49	0.28	2.41	0.04	2.13	0.07

b. The equilibrium solids

As the fractional crystallisation of the samples proceeds, the melt gets increasingly enriched in FeO (Fig. 3, Table S3). The minerals growing out of this melt are therefore increasingly Fe-enriched themselves. This is seen in our experiments, with a continuous chemical composition trend going from grains close to the rim to those close to the core. However, the Fe-Mg exchange coefficient K_D (see main text) between bridgmanite and ferropericlasite is relatively constant across this gradient (Fig. S3) and in agreement with the expected values of ~ 0.6 for pyrolite and ~ 0.3 for olivine (Piet et al., 2016). As ferropericlasite gets richer in iron, so does bridgmanite, and in the same proportion, which is probably the best indication of local thermodynamic equilibrium between the two phases and with the melt they are growing out from.

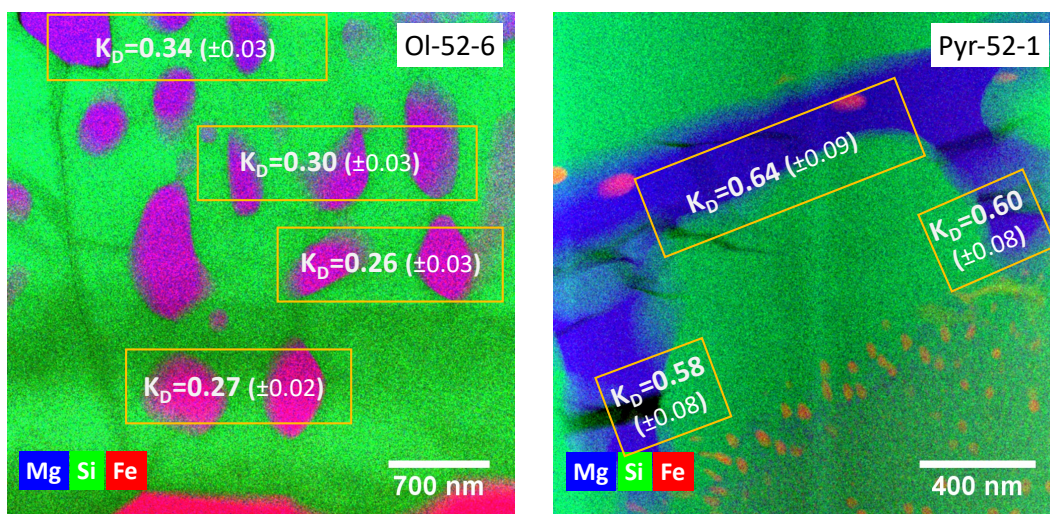


Figure S3: Fe exchange coefficient (K_D) between Brg and Fp in the equilibrium solids (shell) of Ol-52-6 (left) and Pyr-52-1 (right), along with uncertainties. K_D is measured in different radial positions (going from the rim towards the core) for each sample. Because the minerals are fractionally crystallising from an increasingly iron-enriched melt, they are also becoming iron-enriched themselves, and their Fe/Mg increases. However, their K_D is relatively stable and constant within analytical uncertainties, and is equal to what is expected at these pressures [Piet et al., 2016], and also to what is measured in the non-molten subsolidus portion of the sample, *i.e.* 0.3 for olivine and 0.6 for pyrolite. This provides additional support that these phases are crystallising at equilibrium from the melt.

c. The residual melt

The central core contains grains so small (below ~ 100 nm) that they can only be observed by high-resolution TEM analysis (Fig. S4). These are typically a quench feature, produced during rapid quench of the sample, and radically different in size and morphology from the solids crystallising during slow cooling of the experiments (*e.g.*, rim and shell).

Three phases are observed in the samples with a high residual melt fractions (Ol-52-1, Pyr-52-0, and Pyr-52-1); bridgmanite and ferropericlasite forming 10–20 nm thick alternating lamellas typical of a eutectic structure, and iron nanoparticles, sprinkled throughout the melt (Fig. S4). The characterization of these nanoparticles is not straightforward due to their small

size and overlap with the silicate matrix. Nevertheless, the decrease in the oxygen x-ray peak and their very strong nickel enrichment points to a metallic alloy rather than an oxide, a sign of disproportionation recently observed [Armstrong *et al.*, 2019] in silicate melts at high pressures.

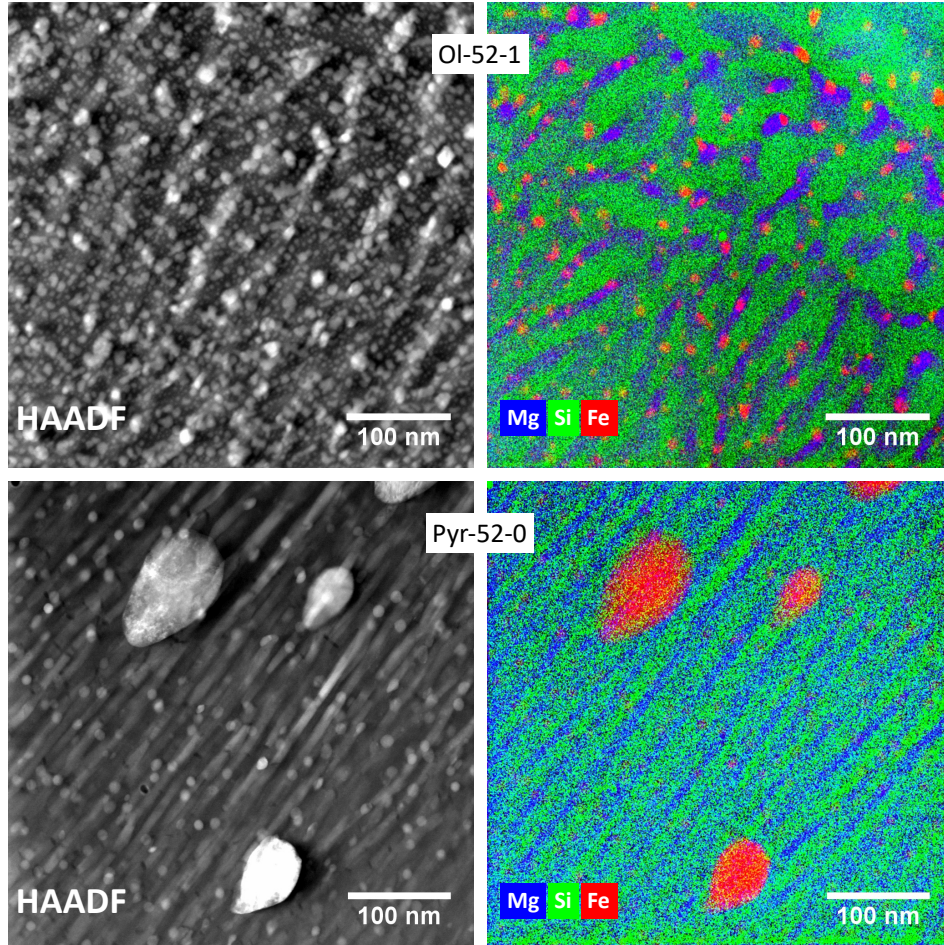


Figure S4: HAADF image and the combined EDS maps of Fe, Mg, and Si from the residual melt (core) region of Ol-52-1 and Pyr-52-0 samples. These show the eutectoid quench textures of Brg (green) and Fp (blue), swarming with metallic iron blobs, a sign of iron disproportionation in the melt, as recently observed by [Armstrong *et al.*, 2019].

The sample with a low residual melt fraction (Ol-52-6) is different in that respect. The melt is so iron-enriched that the iron nanoparticles are much less frequent, but have coalesced in a small individualized blob that can readily be seen in the FIB-EDS analysis (Fig. 1). This leads to an under-estimation of the FeO content of the melt, because such individual blobs concentrate a significant fraction of the iron and some of them can be unsampled during TEM mapping and compositional averaging.

3. Thermodynamic Modelling

We used the model of [Boukare *et al.*, 2015] that solves solid-liquid thermodynamic equilibrium self-consistently. Self-consistency implies that all thermodynamic quantities such as melting temperature, density, and composition of the phases, are linked by thermodynamic rules and thus cannot be fitted independently. The model is based on the computation of end-member chemical potentials. All chemical potentials are taken from previous studies (see [Boukare *et al.*, 2015] and reference therein). At a given pressure, chemical potentials vary with temperature and composition. The code used in [Boukare *et al.*, 2015] finds the temperature at which a liquid of a given composition is equilibrium with a solid (see equation 18-20 in [Boukare *et al.*, 2015]). The result of the calculation is the phase diagram depicted in Fig. 3. From this phase diagram, an ideal fractional crystallization/melting sequence can be computed (Fig. 4) by removing from the melt an infinitesimal amount of the solid that is in equilibrium with this melt.

The thermodynamic model is built on the assumption that the ternary model (FeO-MgO-SiO₂) can be explained from mixing relations in binaries (*i.e.*, MgO-FeO and MgO-SiO₂). This is a strong assumption that needs to be tested, and our experiments provide the necessary tests. Our data show that the thermodynamics of [Boukare *et al.*, 2015] is qualitatively correct, but needs to be recalibrated quantitatively. Indeed, the model in its present form reproduces several major evidences of a fractional melting sequence: the composition of the three phases (Fp, Brg and the melt) during melting/solidification, the order of the appearance of the phases, the position of the cotectic melt line, the modal abundance of minerals in the equilibrium solids, and the modal abundance of liquidus phase solidifying from the melt. However, the comparison fails quantitatively in predicting temperatures (these can be off by as much as 600 K at all pressures), which can be seen in the predicted isotherms in Fig. S8. The predicted cotectic line is also systematically more SiO₂-depleted, with a difference of less than 5%, which can be seen from the offset between the experimental data (yellow points) and the calculation (yellow line) in Fig. 2 and Fig. S8.

Here, we deliberately decided to not readjust the thermodynamics. It is clear that the model and the experimental data are independent from each other. Adjusting the thermodynamics requires similar experiments at various pressures, which are unavailable to date. This is due to thermodynamical self-consistency, where one cannot adjust a parameter independently of the other parameters it is thermodynamically linked to. The only solution is to replicate our measurements made at 52 GPa at one of two higher pressures.

One way out of this, of course, is to break thermodynamic self-consistency, which gives all the adjustable parameters needed to fit the model to the data; but that is meaningless, because it is not extrapolatable to any other pressure, and hence, we deliberately choose not to do that. A qualitatively accurate thermodynamic model which is correct is better than an *ad hoc* fit to the data that bears no thermodynamic sense. It is the aim of our future studies to determine the phase diagrams at different pressures, and then refit the thermodynamical model with that all-encompassing data in hand.

4. Composition of the phases

Table S3: Composition of phases from TEM-EDS quantification (only Ol-52-3 was obtained from SEM-EDS quantification, notice the much larger uncertainties there). The uncertainties are larger than the analytical uncertainty and reflects the standard deviation on multiple analyses. Compositions are in molar fractions. FeO denotes the total iron composition including Fe^{3+} , and metallic iron. In samples that have crystallised to a large fraction (Ol-52-6 and to a lesser degree Ol-52-3), there is a chemical gradient in the shell (Fp and Brg getting iron-enriched as one goes from the rim towards the core). This is due to changes in melt composition, that evolves continuously towards iron enrichment as crystallisation proceeds. The compositions reported here correspond to the measurements closest to the melt, and therefore the ones most relevant to each sample's final stage of crystallisation. This data can be found online in a FAIR-compliant data repository at doi://10.5281/zenodo.4656784

Sample	Melt bulk composition	Residual melt fraction	Phase	Mineral	Composition (mol%)																	
					MgO		σ		FeO		σ		SiO2		σ		Al2O3		σ		CaO	
Ol-52-1	Olivine	50%	Liquidus	Fp	93.2	0.7	6.8	0.7														
			Equilibrium	Brg	46.1	0.4	2.1	0.2	51.8	0.5												
				Fp	90.8	0.7	9.2	0.7														
			Melt		50.5	0.5	10	0.3	39.5	0.2												
Ol-52-3	Olivine	20%	Liquidus	Fp	86.9	3.7	13.1	3.7														
			Equilibrium	Brg	47.3	2.6	4.2	2.8	48.5	2.9												
				Fp	76	5.5	24	5.5														
			Melt		39.8	0.7	27.6	2.1	32.6	1.5												
Ol-52-6	Olivine	2%	Liquidus	Fp	92	0.5	8	0.5														
			Equilibrium	Brg	44.5	0.2	4.4	0.1	51.1	0.2												
				Fp	73.5	0.3	26.5	0.3														
			Melt		32.8	1.3	37.5	0.3	29.7	1												
Pyr-52-0	Pyrolite	50%	Liquidus	Brg	44.0	0.4	1.7	0.1	49.8	0.1	2.6	0.2	1.9	0.2								
			Equilibrium	Brg	42.5	0.4	2.6	0.1	48.5	0.5	3.2	0.1	3.2	0.2								
				Fp	92	0.6	8	0.6														
			Melt		43.0	0.3	14.8	0.5	36.3	0.1	3.1	0.2	2.9	0.3								
Pyr-52-1	Pyrolite	50%	Liquidus	Brg	44.2	0.9	1.9	0.2	48.9	0.9	2.8	0.2	2.2	0.2								
			Equilibrium	Brg	43.0	1.3	2.4	0.3	49.6	0.7	2.8	0.3	2.3	0.4								
				Fp	91.9	1.5	8.2	1.5														
			Melt		42.4	1.8	14.2	1.6	36.7	0.3	3.4	0.1	3.3	0.2								

Sample	Melt bulk composition	Pressure (GPa)	Phase	Mineral	Composition (mol%)									
					MgO		FeO		SiO2		Al2O3		CaO	
Pyr-52-0	Pyrolite	52	Liquidus	Brg	44.0	0.4	1.7	0.1	49.8	0.1	2.6	0.2	1.9	0.2
Pyr-52-1	Pyrolite	52	Liquidus	Brg	44.2	0.9	1.9	0.2	48.9	0.9	2.8	0.2	2.2	0.2
Pyr-85-0	Pyrolite	85	Liquidus	Brg	44.5	0.3	1.3	0.1	50.5	0.3	1.9	0.2	1.9	0.1
Pyr-129-0	Pyrolite	129	Liquidus	Brg	43.4	0.8	1.6	0.2	51.0	0.7	2.0	0.4	2.0	0.1

5. Comparison with previous melting experiments in the LHDAC

While our experimental protocol relies on the controlled fractional crystallisation of a melt in the LHDAC, our results can be compared to those from recent studies of melting in the LHDAC. Our observation of iron-enrichment in the melt is fully consistent with recent LHDAC studies of mantle melting [Fiquet *et al.*, 2010; Nomura *et al.*, 2011; Pradhan *et al.*, 2015], all based on sample recovery and *ex situ* chemical analysis. This corpus of work stands in stark discrepancy with an *in situ* study [Andrault *et al.*, 2012] of melt composition, that comes to the opposite conclusion. *In situ* analyses should however be interpreted cautiously, because despite their narrow lateral size, *in situ* x-ray beams axially sample the full concentric shell structure of the melt pocket; they stack (and sample) a two-dimensional projection of an intrinsically three-dimensional object (Fig. 1, Fig. S5, Fig. S9). Regardless of how narrow (laterally) the x-ray beams are, the parts of the rim (liquidus phase) and shell (equilibrium phases) that lie below and above the central core (residual melt) unavoidably add their signal and can strongly bias the chemical signature of the melt.

6. Additional Figures

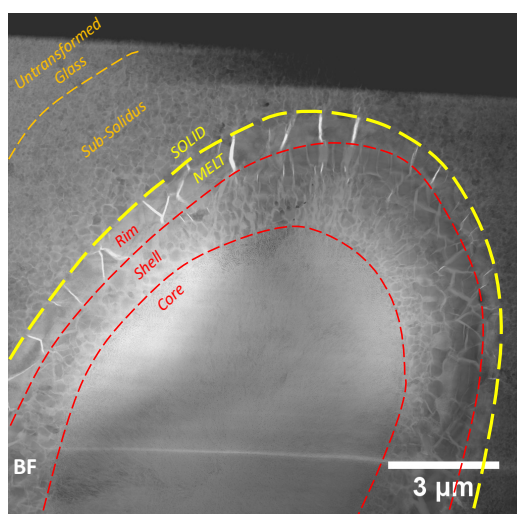


Figure S5: TEM bright field image showing overview of Ol-52-1 sample; the center of the sample is clearly seen along with the spherical geometry of the assemblage (deformed to an ellipsoid, with the short axis parallel to the compression axis in the LHDAC). The yellow line separates the melt pocket from the rest of the sample. The melt pocket is the only part that has undergone melting and differentiation. Everything outside is either untransformed glass (far away from the melt), or a sub-solidus assemblage in the vicinity of the melt, that is due to the glass recrystallizing at high temperature. It has the same composition as the untransformed glass, and the same as the starting material. Therefore, there is no chemical interaction between the melt pocket and the outside, and the “yellow” dashed line in the figure is impermeable. The melt pocket is effectively a closed system.

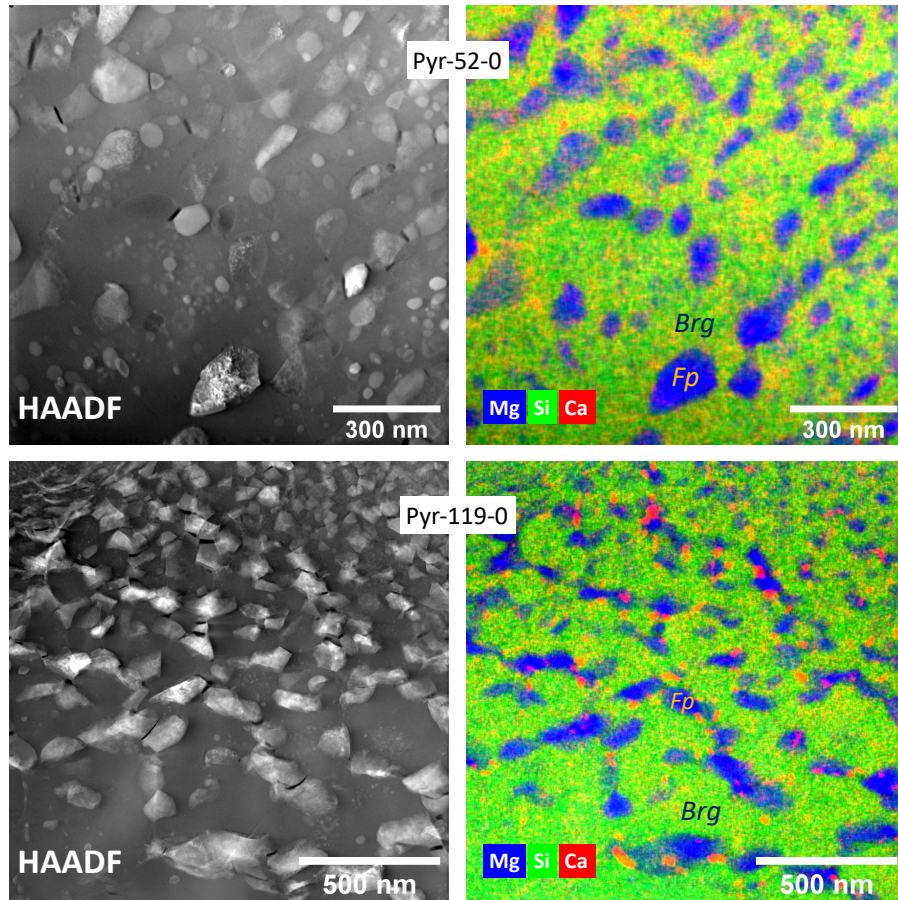


Figure S6: HAADF image (left) and the combined EDS maps of Mg, Si, and Ca (right) from the sub-solidus regions of the Pyr-52-0 (top) and Pyr-119-0 (bottom) samples. The subsolidus region is composed of ferropericlasite (Fp, blue grains), bridgmanite (Brg, green grains) and calcium silicate perovskite (CaPv, red grains), as expected in those P-T conditions. The overall composition in this region is the same as the starting composition (Table S1).

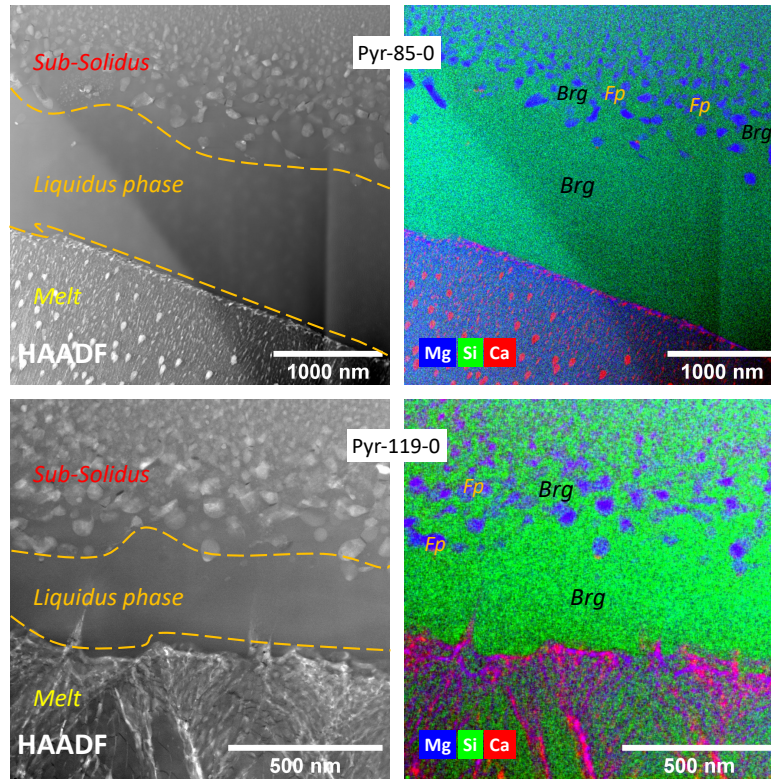


Figure S7: TEM images (left) and chemical maps (right) of the higher pressure samples molten at 85 GPa (top) and 129 GPa (bottom). These are produced with very short crystallisation times (< 10 seconds, see Fig. S1) to retain a large fraction of residual melt, and only crystallise the liquidus phase (Brg). That is because these experiments were performed to analyse the composition of liquidus Brg and to address the issue of Calcium incorporation in that phase at higher pressures. Note that as expected in this case, the equilibrium solids have not crystallised in these samples, and the residual melt has not reached the cotectic composition.

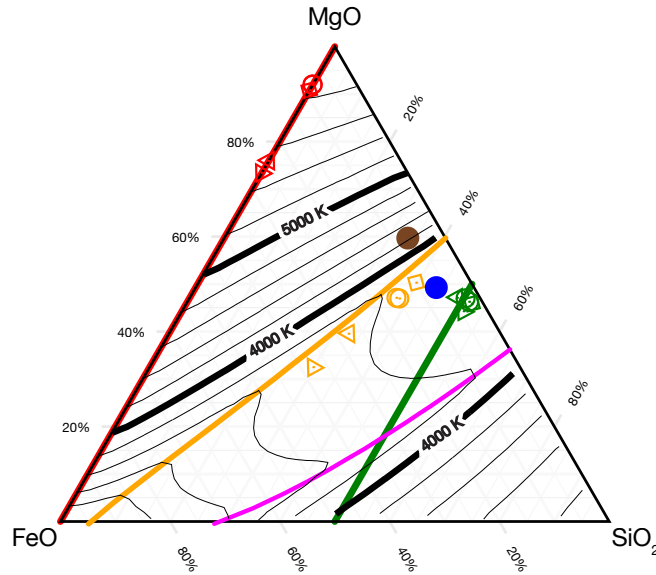


Figure S8: The same phase diagram as in Fig. 3, with an overlay of the liquidus isotherms, calculated according to [Boukare *et al.*, 2015]. The maroon and blue circles represent the olivine and pyrolytic starting compositions, respectively. Melt compositions are plotted as yellow symbols. Red and green symbols represent the compositions of ferropericlasite and bridgmanite measured in the equilibrium solids.

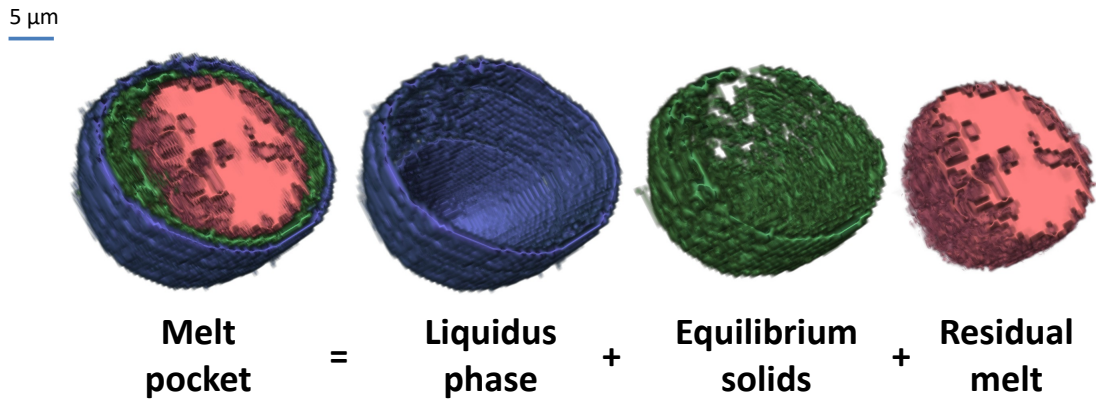


Figure S9: Chemical segmentation and phase separation. The figure shows the 3D deconstruction of the whole (Ol-52-1 in Fig 1) sample, as well as its constitutive rim (Fp), shell (mainly Brg), and melt core.

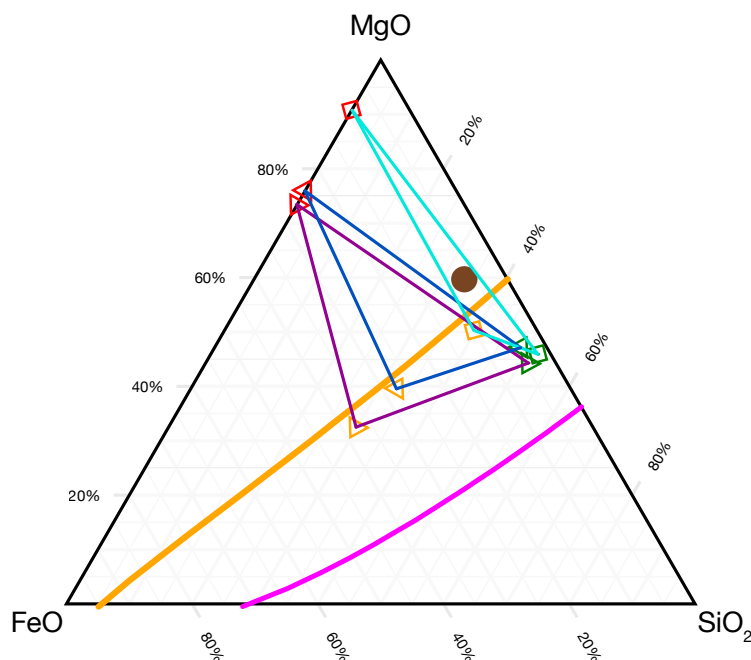


Figure S10: If pure batch crystallisation were to take place (in the case of a bulk olivine melt composition here), mass balance imposes that the bulk composition (brown circle) must always lie within the Fp–Brg–Melt triangle. It can therefore be graphically demonstrated that the occurrence of pure batch melting is impossible in our experiments. While the Ol-52-1 experiment (light blue triangle) could potentially be the result of batch crystallisation (because the bulk composition lies inside the triangle), the Ol-52-3 (dark blue) and Ol-52-6 (violet) experiments violate the mass balance rule with the starting composition sitting outside of their respective triangles. In batch melting, when the join between the two solid phases crosses the bulk composition, then all melt is extinguished, and this cannot possibly produce Fp phases and residual melts as enriched in iron as observed.

7. References

- Akahama, Y., and H. Kawamura (2010), Pressure calibration of diamond anvil Raman gauge to 410 GPa., *215*, 012195, doi:10.1088/1742-6596/215/1/012195.
- Andrault, D., S. Petitgirard, G. Lo Nigro, J. L. Devidal, G. Veronesi, G. Garbarino, and M. Mezouar (2012), Solid-liquid iron partitioning in Earth's deep mantle, *Nature*, *487*(7407), 354—, doi:10.1038/nature11294.
- Armstrong, K., D. J. Frost, C. A. McCammon, D. C. Rubie, and T. Boffa Ballaran (2019), Deep magma ocean formation set the oxidation state of Earth's mantle, *Science*, *365*(6456), 903–906, doi:10.1126/science.aax8376.
- Boukare, C. E., Y. Ricard, and G. Fiquet (2015), Thermodynamics of the MgO-FeO-SiO₂ system up to 140 GPa: Application to the crystallization of Earth's magma ocean, *J. Geophys. Res.*, *120*(9), 6085–6101, doi:10.1002/2015JB011929.
- Fiquet, G., A. L. Auzende, J. Siebert, A. Corgne, H. Bureau, H. Ozawa, and G. Garbarino (2010), Melting of Peridotite to 140 Gigapascals, *Science*, *329*(5998), 1516–1518, doi:10.1126/science.1192448.
- Nomura, R., H. Ozawa, S. Tateno, K. Hirose, J. Hernlund, S. Muto, H. Ishii, and N. Hiraoka (2011), Spin crossover and iron-rich silicate melt in the Earth's deep mantle, *Nature*, *473*(7346), 199–202, doi:10.1038/nature09940.
- Piet, H., J. Badro, F. Nabiei, T. Dennenwaldt, S.-H. Shim, M. Cantoni, C. Hébert, and P. Gillet (2016), Spin and valence dependence of iron partitioning in Earth's deep mantle, *P Natl Acad Sci USA*, *113*(40), 11127–11130, doi:10.1073/pnas.1605290113.
- Pradhan, G. K., G. Fiquet, J. Siebert, A. L. Auzende, G. Morard, D. Antonangeli, and G. Garbarino (2015), Melting of MORB at core-mantle boundary, *Earth Planet Sc Lett*, *431*, 247–255, doi:10.1016/j.epsl.2015.09.034.